


RESEARCH ARTICLE

Simultaneous whole-liver water T_1 and T_2 mapping with isotropic resolution during free-breathing

Jonathan Stelter¹  | Kilian Weiss² | Lisa Steinhelfer¹ | Veronika Spieker^{3,4} | Elizabeth Huaroc Moquillaza¹ | Weitong Zhang⁵ | Marcus R. Makowski¹ | Julia A. Schnabel^{3,4,6} | Bernhard Kainz^{5,7} | Rickmer F. Braren¹ | Dimitrios C. Karampinos^{1,8,9}

¹Institute of Diagnostic and Interventional Radiology, School of Medicine and Health, Technical University of Munich, Munich, Germany

²Philips GmbH Market DACH, Hamburg, Germany

³Institute of Machine Learning for Biomedical Imaging, Helmholtz Munich, Neuherberg, Germany

⁴School of Computation, Information and Technology, Technical University of Munich, Munich, Germany

⁵Department of Computing, Imperial College London, London, United Kingdom

⁶School of Biomedical Imaging and Imaging Sciences, King's College London, London, United Kingdom

⁷Department Artificial Intelligence in Biomedical Engineering, Friedrich-Alexander-Universität Erlangen-Nürnberg (FAU), Erlangen, Germany

⁸Munich Institute of Biomedical Engineering, Technical University of Munich, Garching, Germany

⁹Munich Data Science Institute, Technical University of Munich, Garching, Germany

Correspondence

Jonathan Stelter, Institute of Diagnostic and Interventional Radiology, School of Medicine and Health, Ismaninger Str. 22, 81675 Munich, Germany.

Email: jonathan.stelter@tum.de

Funding information

Philips Healthcare; TUM International Graduate School of Science and Engineering

Abstract

Purpose: To develop and validate a data acquisition scheme combined with a motion-resolved reconstruction and dictionary-matching-based parameter estimation to enable free-breathing isotropic resolution self-navigated whole-liver simultaneous water-specific T_1 (wT_1) and T_2 (wT_2) mapping for the characterization of diffuse and oncological liver diseases.

Methods: The proposed data acquisition consists of a magnetization preparation pulse and a two-echo gradient echo readout with a radial stack-of-stars trajectory, repeated with different preparations to achieve different T_1 and T_2 contrasts in a fixed acquisition time of 6 min. Regularized reconstruction was performed using self-navigation to account for motion during the free-breathing acquisition, followed by water-fat separation. Bloch simulations of the sequence were applied to optimize the sequence timing for B_1 insensitivity at 3 T, to correct for relaxation-induced blurring, and to map T_1 and T_2 using a dictionary. The proposed method was validated on a water-fat phantom with varying relaxation properties and in 10 volunteers against

Abbreviations: BIR, B_1 -insensitive rotation; F/H, feet-head; GRASE, gradient and spin echo; MOLLI, modified Look-Locker inversion recovery; MRF, MR fingerprinting; PCA, principal component analysis; PDFF, proton density fat fraction; PRESS, point resolved spectroscopy; SHORTIE, short- T_R multi- T_1 multi- T_E STEAM; STEAM, stimulated echo acquisition mode; TV, total variation; VFA, variable flip angle; wT_1 , water-specific T_1 ; wT_2 , water-specific T_2 .

This is an open access article under the terms of the [Creative Commons Attribution](https://creativecommons.org/licenses/by/4.0/) License, which permits use, distribution and reproduction in any medium, provided the original work is properly cited.

© 2024 The Author(s). *NMR in Biomedicine* published by John Wiley & Sons Ltd.

imaging and spectroscopy reference values. The performance and robustness of the proposed method were evaluated in five patients with abdominal pathologies.

Results: Simulations demonstrate good B_1 insensitivity of the proposed method in measuring T_1 and T_2 values. The proposed method produces co-registered wT_1 and wT_2 maps with a good agreement with reference methods (phantom: $wT_1 = 1.02wT_{1,ref} - 8.93\text{ms}$, $R^2 = 0.991$; $wT_2 = 1.03wT_{2,ref} + 0.73\text{ms}$, $R^2 = 0.995$). The proposed wT_1 and wT_2 mapping exhibits good repeatability and can be robustly performed in patients with pathologies.

Conclusions: The proposed method allows whole-liver wT_1 and wT_2 quantification with high accuracy at isotropic resolution in a fixed acquisition time during free-breathing.

KEYWORDS

BIR-4 preparation, dictionary matching, radial stack-of-stars, relaxometry, water-fat separation

1 | INTRODUCTION

The prevalence of chronic liver disease is increasing worldwide, with steatotic liver diseases (SLDs) being one of the primary causes, closely linked to modern lifestyle patterns and unhealthy eating habits.^{1–3} Chronic liver disease is associated with various pathologies, including liver inflammation, cirrhosis, and hepatocellular carcinoma.⁴

Quantitative MRI has emerged as a promising non-invasive approach for assessing chronic liver diseases, mitigating the need for expensive and potentially risky liver biopsies.^{5,6} Proton density fat fraction (PDFF) is a widely used biomarker for quantification of liver fat content,^{7,8} while R_2^* is associated with the liver iron content,^{9,10} and MR elastography can measure liver stiffness and fibrosis.¹¹ T_1 mapping methods have also gained interest because T_1 relaxation has been shown to be associated with liver inflammation and fibrosis^{12–14} and might offer the advantage of not requiring a complex setup compared with MR elastography.¹⁵ T_2 mapping has been extensively studied and validated in various tissues, such as myocardium^{16,17} and skeletal muscle.¹⁸ While studies^{13,14,19–23} have shown applications of T_2 mapping in the liver, future studies with optimized liver sequences are unavoidable to evaluate its whole potential.

Conventional T_1 and T_2 mapping methods (e.g., modified Look-Locker inversion recovery (MOLL)²⁴ and multi-echo spin echo for T_1 and T_2 mapping, respectively) usually rely on single-slice acquisitions in combination with breath-holds to avoid respiratory motion artifacts and may be confounded by the presence of fat.²⁵ However, breath-hold scans may not be feasible for all patients and do not permit whole-liver assessment of focal lesions or structural changes due to their limited slice coverage. Variable flip angle (VFA) methods have been introduced for time-efficient volumetric mapping of liver T_1 relaxation in a single or multiple breath-holds.^{26–29} VFA methods are based on gradient-echo acquisitions with different excitation flip angles. Therefore, VFA methods show a considerable sensitivity to transmit B_1 inhomogeneities³⁰ and may require additional B_1 mapping.³¹

Recently, methods have been proposed to acquire volumetric water-specific T_1 (wT_1) maps of the whole liver during a free-breathing acquisition,^{32,33} typically employing Dixon imaging to achieve robust fat suppression. These methods frequently rely on a motion-robust radial stack-of-stars k -space trajectory and perform a respiratory-motion-informed reconstruction using an external motion sensor³² or additional MR navigator signals.³³ While previous works mainly focus on the quantification of wT_1 or the simultaneous quantification of wT_1 , PDFF and R_2^* ,^{27,29,33,34} simultaneous wT_1 and water-specific T_2 (wT_2) mapping not only provides co-registered maps but also crucially allows for the correction of T_1 as a confounding factor in T2prep- and gradient echo-based T_2 mapping.^{35–38} Free-breathing liver T_1 mapping methods usually rely on a Look-Locker scheme acquiring many different inversion contrasts after one inversion pulse. However, combining this scheme with T_2 mapping may not be straightforward. Furthermore, the Look-Locker acquisition scheme combined with a radial stack-of-stars trajectory restricts the resolution in the partition encoding direction and impedes the self-navigation ability of the trajectory due to the varying contrast along k_z projections.³² Volumetric, wT_1 , and wT_2 mapping of the whole liver with isotropic resolution enables characterization of the spatial distribution of liver inflammation and fibrosis in relation to the liver segments and of their relationship to hepatocellular carcinoma.^{33,39} There is preliminary work on the simultaneous mapping of T_1 and T_2 at isotropic resolution using a variable density Cartesian trajectory and navigators at 1.5 T.⁴⁰ Previous works on free-breathing volumetric T_1 mapping at 3 T rely on acquiring data for two different flip angles^{41,42} or use an adiabatic inversion pulse combined with a B_1 -accounted subspace reconstruction³² to minimize errors due to B_1 inhomogeneities, although Look-Locker techniques are usually more robust in the presence of B_1 inhomogeneities compared with VFA methods.⁴³

The purpose of the present work is to develop a method for free-breathing isotropic resolution self-navigated B_1 -insensitive whole-liver simultaneous wT_1 and wT_2 mapping based on the radial stack-of-stars trajectory.

2 | METHODS

2.1 | Pulse sequence

A magnetization-prepared spoiled gradient echo sequence that is insensitive to B_1 was developed for encoding T_1 and T_2 . The pulse sequence comprises an adiabatic modified B_1 -insensitive rotation (BIR)-4 preparation pulse (frequency sweep = 3700 Hz, amplitude = 13.5 μ T, and duration without gap = 10 ms)^{38,44,45} with a variable gap duration between the BIR-4 segments (T_{prep}). A variable pulse angle (T2prep with $\phi = 0^\circ$ and T1prep with $\phi = 180^\circ$) is employed to achieve either a 0° (T_2 -) or a 180° (inversion) preparation using the same preparation module. The preparation is followed by a two-echo bipolar gradient echo stack-of-stars readout. Radial spokes are acquired with pseudo-golden-angle ordering⁴⁶ in the k_x - k_y -plane, and centric profile ordering is employed along the partition encoding direction k_z (see Figure 1). In each shot, profiles along the k_z direction are read out at a fixed angle, and partial Fourier encoding is applied along the k_z direction. The delay time between the preparation pulse and readout (T_{delay}) and the waiting time between two shots (T_{wait}) are variable per preparation. In total, four different preparations ($2 \times T1_{\text{prep}}, 2 \times T2_{\text{prep}}$) are acquired. It has been previously shown that liver T_1 and T_2 mapping based on a limited number of preparations is feasible when employing dictionary matching for parameter mapping.^{40,47,48}

To minimize the B_1 sensitivity of T_1 and T_2 parameter estimation while reducing acquisition time, T_{delay} and T_{wait} were optimized using a grid search. Bloch simulations were carried out to simulate the signal for varying transmit B_1 values ($B_1 = [0.75, 1, 1.25]$), and T_1 and T_2 estimates were

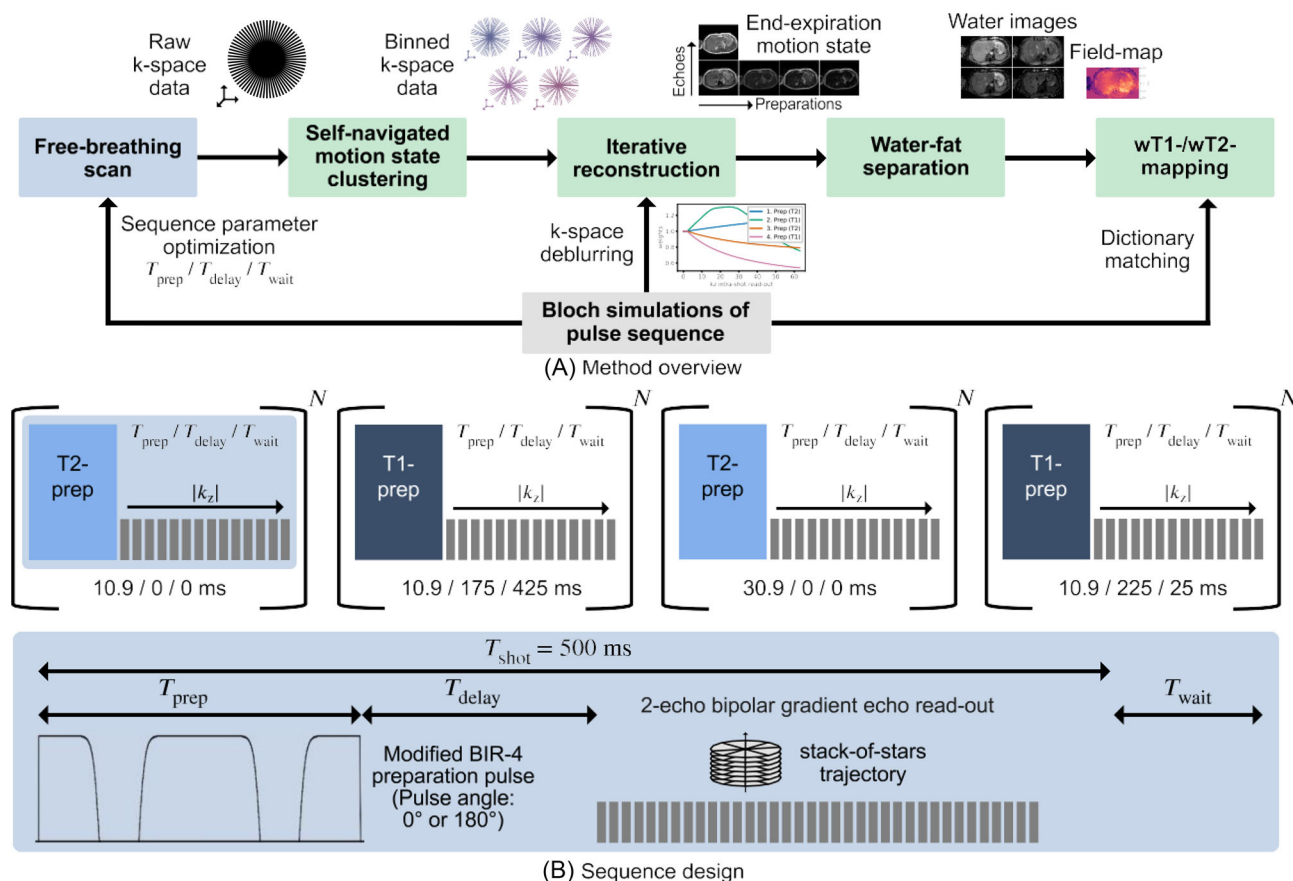


FIGURE 1 A, Overview of the proposed method for simultaneous wT_1 and wT_2 mapping consisting of a free-breathing magnetization-prepared data acquisition combined with a self-navigated motion-resolved reconstruction and parameter mapping using dictionary matching on fat-suppressed images. B, The sequence involves four distinct preparations, with each preparation consisting of N shots. Each shot begins with an adiabatic preparation pulse, followed by a two-echo gradient echo readout that encodes the k_z direction. For each shot, the angle of the radial spokes is varied.

calculated through dictionary matching assuming $B_1 = 1$. The minimum of the combined T_1 and T_2 error, ξ , and minimized acquisition time, T_{acq} , were determined based on an L-curve plot (Supplementary Figure S1):

$$\xi = \sqrt{\frac{\sum_i N_{B_1} N_{T_1} N_{T_2} \left(\frac{T_{1j} - \tilde{T}_{1j}}{\Delta T_1} \right)^2 + \left(\frac{T_{2j} - \tilde{T}_{2j}}{\Delta T_2} \right)^2}{N_{B_1} N_{T_1} N_{T_2}}} \quad (1)$$

$$T_{\text{acq}} = \sum_i^4 T_{\text{shot}} + T_{\text{wait},i} \quad (2)$$

with $N_{B_1} N_{T_1} N_{T_2}$ the number of simulated signals with different B_1 , T_1 , and T_2 ($T_1 = [600, 850, 1200]$ ms, $T_2 = [20, 40, 60]$ ms); T_{ij} and \tilde{T}_{ij} denote the simulated and estimated relaxation times, respectively, while ΔT_j refers to the dictionary step size and introduces a normalization for the error metric with respect to the relaxation times ($\Delta T_1 = 40$ ms, $\Delta T_2 = 3$ ms).

2.2 | Image reconstruction and parameter quantification

In addition to the pulse sequence, the proposed method introduces a four-step reconstruction and quantification framework consisting of (1) a self-navigation-based motion state estimation, (2) a motion-resolved image reconstruction, (3) a graph-cut-based water-fat separation, and (4) wT_1 and wT_2 mapping using dictionary matching based on Bloch simulations.

2.2.1 | Motion state estimation

The k -space center along the k_z direction was selected, corresponding to the center of each radial spoke. An inverse Fourier transform was performed along the k_z direction, and an eddy-current correction was applied.⁴⁹ The k_z , echo, and coil dimensions were combined into the sample dimension, while the spoke and preparation dimensions were combined into the time dimension. The temporal resolution is given by the shot duration and waiting time, which is around 500 ms for the T_2 preparations. The magnitude and phase information were processed individually and concatenated along the sample dimension. First, the intensity was normalized using the maximum and minimum value for each preparation and sample. Second, the data was centered around zero using the median value. Principal component analysis (PCA) was subsequently performed along the time dimension.⁵⁰ The component from the first two components that had the highest peak in the 0.1–0.5 Hz frequency range was selected, as it likely represents the respiratory motion. The estimated motion curve $\tilde{m}(t)$ was rescaled with $p_{i,\min}$ the 5th percentile and $p_{i,\max}$ the 95th percentile per preparation i :

$$m_i(t) = \frac{\tilde{m}_i(t) - p_{i,\min}}{p_{i,\max} - p_{i,\min}} \quad (3)$$

Five equally spaced motion states were defined based on the amplitude of $m(t)$ corresponding to the relative displacement (center of the bins: [0.1, 0.3, 0.5, 0.7, 0.9]). In this study, the end-expiration state and the adjacent motion state were used in the iterative reconstruction to reconstruct volumes for two different motion states, using regularization over the motion state dimension. Water-fat separation and parameter mapping were only performed for the end-expiration state, as the dynamic information is usually not considered important for diagnosis. A complete reconstruction of all five motion states is given in Figure S11 for reference.

2.2.2 | Image reconstruction

T_1 relaxation of the prepared magnetization occurs during the readout of the k_z direction in a single shot, resulting in blurring along the feet-head (F/H) axis in the reconstructed images (Supplementary Figure S3). To alleviate the relaxation-induced blurring, the k -space profile j in the k_z direction was multiplied by a filter, H_{ij} , for each preparation i . The filter weights were determined through Bloch simulations of the sequence. The average signal curve \bar{s}_{ij} was estimated for a range of relaxation times ($T_1 = 200:300:1700$ ms, $T_2 = 20:10:60$ ms). The curve was then normalized to the transverse magnetization in the vicinity of the k -space center acquisition ($j = -1$ for $k_z = -\Delta k_z$), and the inverse was computed for the outer k -space profiles:

$$H_{ij} = \begin{cases} 1, & \text{if } j \in \{0, 1, -1\} \\ \bar{s}_{i,-1}/\bar{s}_{ij}, & \text{otherwise.} \end{cases} \quad (4)$$

The inverse reconstruction problem was solved iteratively for the 3D volume using an alternating direction method of multipliers (ADMM) optimizer:

$$x = \underset{x'}{\operatorname{argmin}} \|\mathcal{F}Sx' - y\|_2^2 + \mathcal{R}(x') \quad (5)$$

$$\mathcal{R}(x) = \alpha_1 \|\operatorname{TV}_{\text{temporal}}(x)\|_1 + \alpha_2 \|\operatorname{TV}_{\text{spatial}}(x)\|_1 \quad (6)$$

with x the complex reconstructed images for the preparations, motion states and echoes, y the motion state-binned multi-coil k -space, \mathcal{F} the inverse Fourier transform along the k_z direction and the non-uniform fast Fourier transform per slice, S the ESPIRiT coil sensitivity maps,⁵¹ and \mathcal{R} the regularization term.

Two total variation (TV) regularizers were incorporated to ensure efficient convergence. First, TV regularization along the motion state dimension was used to ensure smooth transitions between different motion states for every voxel⁵⁰ using a direct algorithm.⁵² Second, a 3D TV regularizer was applied to further exploit the sparsity in the spatial domain using a fast gradient projection algorithm.⁵³

2.2.3 | Water-fat separation

The two echo images of the end-expiration motion state were further processed to decompose water and fat signals based on a graph-cut algorithm. The multi-resolution graph-cut algorithm for three or more echoes⁵⁴ was combined with a phasor estimation for dual-echo water-fat separation⁵⁵ to compute an unwrapped field-map estimate. The algorithm carries out a graph-cut on various layers with distinct parameters and image resolutions (isotropic voxel sizes: 5.5 mm, 3 mm, and the interpolated voxel size of 1.75 mm) for increased robustness.⁵⁴ The solution from the previous layer served as the initialization to resolve the ambiguity of the separation problem and correct for voxels without a phasor estimate. The field-map of the first preparation (T2prep) functioned as the initialization for the other preparations. Water images were generated based on the field-map estimate.

2.2.4 | wT_1 and wT_2 mapping

A B_0 -specific dictionary was created based on Bloch simulations of the BIR-4 preparation pulse and the gradient echo readout, using the parameters $T_1 = 95:15:2000$ ms, $T_2 = 9:1.5:120$ ms, and $B_0 = -300:10:300$ Hz. B_0 effects were especially considered during the the BIR-4 pulse to remove the effect of B_0 offsets on the magnetization after the preparation.³⁸ The transverse magnetization during the k -space center acquisition was used as a dictionary entry. The normalized water images were voxel-wise matched to the B_0 -specific dictionary to estimate wT_1 and wT_2 maps by minimizing the L2 difference between the simulated and measured signals.

2.3 | Experiments

The proposed wT_1 and wT_2 mapping was compared with different imaging and single-voxel MRS techniques. Single-voxel MRS techniques were employed to specifically measure the relaxation properties of the water component in the presence of fat.^{34,56,57} MOLLI and gradient and spin echo (GRASE) are the vendor's single-slice single-breath-hold or respiratory-triggered techniques for in vivo T_1 or T_2 mapping, respectively. Dixon spin echo is a single echo spin-wrap Dixon spin echo acquisition which is used to measure T_2 due to its insensitivity to stimulated echoes and the ability to remove the fat component. Stimulated echo acquisition mode (STEAM) T_1 is a standard technique for MRS-based measurement of T_1 . However, STEAM T_1 and Dixon spin echo are unsuitable for in vivo use due to their motion sensitivity and lengthy acquisition times. Short- T_R multi- T_1 multi- T_E STEAM (SHORTIE)⁵⁸ T_1 and point resolved spectroscopy (PRESS) T_E are efficient methods for in vivo MRS-based measurement of wT_1 or wT_2 in fat-containing tissues, respectively. In comparison with MOLLI and GRASE, the MRS techniques can be applied as efficient and fat-unconfounded references, as they can be performed in a breath-hold while correcting for the presence of fat.⁵⁹

All measurements were performed on a clinical 3 T scanner (Ingenia Elition X, Philips Healthcare, The Netherlands). The study was approved by local institutional review board (Klinikum rechts der Isar, Technical University of Munich, Munich, Germany). Informed consent was given by

TABLE 1 Sequence parameters used in the phantom experiment and in the volunteer and patient study. The reference T_1 and T_2 mapping techniques, MOLLI and GRASE, can be confounded by the presence of fat, whereas the proposed method and single-voxel MRS sequences can measure the water-specific parameters (wT_1 and wT_2).

Parameter	Imaging scans			Spectroscopy scans			
	Proposed method ^a	GRASE ^b	MOLLI ^b	Dixon spin echo ^c	SHORTIE T_1 ^b	STEAM T_1 ^c	PRESS T_E ^b
Motion compensation	wT_1/wT_2	T_2	T_1	wT_2	wT_1	wT_1	wT_2
Motion compensation	Free-breathing	Triggered	Breath-hold	—	Breath-hold	—	Breath-hold
Voxel size (mm ³)	$3 \times 3 \times 3$ (3D)	$3 \times 3 \times 3$ (2D)	$2 \times 2 \times 5$ (2D)	$2 \times 2 \times 5$ (2D)	Phantom: $10 \times 10 \times 15$ (NSA=2) In vivo: $15 \times 15 \times 15$ (NSA=1)		
FOV (mm ³)	$400 \times 400 \times 200$	$400 \times 400 \times 5$	$400 \times 400 \times 5$	$200 \times 200 \times 5$	—	—	—
T_E (ms)	[1.1,2.2]	[16,24,32,40,48,56,64,72]	1.09	[10,15,20,25,30] ^d	9.8	10	[28,30,35,40,45,50]
T_1 (ms)	[175,225] ^e	—	5(3) ^f with min. T_1 : 113.1/350	—	[10,150,500,800,1000,1200,1500]	[10,100,500,1500,2500]	—
T_R (ms)	3.8	1641	2.32	1000	$\tau = 686.5^g$	5000	1500
FA (°)	8	90	20	90	90	90	90
Acceleration	Radial	SENSE (R = 2)	CS-SENSE (R = 3)	—	—	—	—
	undersampling & partial Fourier ^h						
Scan time (min:s)	6:09	2:24 (nominal)	0:11	5×3:23	0:18	0:40	0:11

^aPhantom, volunteer, and patient study.

^bPhantom and volunteer study.

^cOnly phantom study.

^dDixon multi-acquisition per echo time (T_E) with $\Delta T_E = 1$ ms for second acquisition.

^e T_{delay} for T_1 preparations.

^fMOLLI scheme: 5 s acquisition with first $T_1 = 113.1$ ms, 3 s pause, 3 s acquisition with first $T_1 = 350$ ms.

^g T_R dependent on T_1 , min. $T_R = 725.6$ ms.

^h149 radial angles per preparation and partial Fourier factor in $k_z = 3/4$.

volunteers and patients. Phantom measurements used a 16-channel head coil and in vivo measurements were performed with an anterior coil and posterior coils having 16 and 12 channels, respectively. The proposed wT_1 and wT_2 mapping sequence was acquired with 149 radial angles per preparation and a partial Fourier factor of 3/4 in the partition encoding direction corresponding to a scan time of 6 min 9 s. Sequence parameters are summarized in Table 1. The respiratory signal estimated by the self-navigator was compared with a respiratory motion-tracking camera provided by the vendor (VitalEye, Philips Healthcare, The Netherlands).^{60–63}

2.3.1 | B_1 , fat fraction, and SNR simulation

To evaluate the optimized sequence parameters, the sequence was simulated with $B_1 = 0.6:0.1:1.2$ for different $T_1 = 500:50:1300$ ms and $T_2 = 15:2.5:55$ ms. The simulated transverse magnetization during the acquisition of the k -space center was taken as the signal and matched with the dictionary. The error between the simulated and estimated relaxation parameters was calculated for each combination of parameters.

The performance of the proposed method was further assessed with regard to its sensitivity to fat and noise for a realistic scenario in the presence of B_0 inhomogeneities. A human body model (XCAT phantom, Duke University Medical Center, Durham, NC, USA)⁶⁴ was employed to generate T_1 , T_2 , PDFF and magnetic susceptibility maps. Physical realistic relaxation times at 3T and magnetic susceptibilities were assigned to organs in the abdomen.^{65–67} T_2^* relaxation was neglected, as two echoes with short echo times were simulated. The liver T_1 and T_2 were set to 800 ms and 25 ms, respectively. The liver PDFF and SNR were varied from 0 to 50% and 50 to 300, respectively. The field-map f_B was simulated by computing the convolution between a dipole kernel and the magnetic susceptibility map. Water and fat images were computed using the entries of the B_0 -specific dictionary. Complex MR images were simulated based on a water–fat signal model^{68,69} assuming a multi-peak fat model. Different SNR levels were simulated by adding Gaussian noise to the real and imaginary images.

To evaluate the proposed method, water–fat separation and dictionary matching was performed, similar to the phantom and in vivo measurements. For the segmented liver, the mean difference between the reference value and the estimated wT_1 and wT_2 and the standard deviation were calculated.

2.3.2 | Phantom measurements

The parameter quantification was validated using two different phantoms. The T_1 phantom is a water–fat phantom (Calimatrix, Madison, WI, USA) composed of 12 vials with varying wT_1 (approximate range: from 500 ms to 1200 ms) and fat fraction (approximate range: from 0% to 11%). The custom-built T_2 phantom contains six vials with varying wT_2 (approximate range: from 10 ms to 40 ms) and also varying wT_1 (approximate range: from 100 ms to 1600 ms) due to different concentrations of manganese(II) chloride ($c \in [0, 0.05, 0.2, 0.35, 0.5]$ mM). One vial ($c = 0.2$ mM) has a fat fraction of about 32% whereas the other vials do not contain fat.

Parameter estimates from the proposed method, MOLLI, and GRASE imaging techniques, as well as SHORTIE T_1 and PRESS T_E spectroscopy techniques, were validated against STEAM T_1 (wT_1 reference) and Dixon spin echo (wT_2 reference) techniques.

2.3.3 | Volunteer measurements

Ten volunteers were scanned in the study, where the proposed method was compared with GRASE and MOLLI techniques, and SHORTIE T_1 and PRESS T_E as spectroscopy references. Three MRS voxels were placed through the liver. The proposed method was repeated one more time for five volunteers after the entire scan protocol without repositioning to assess the repeatability of the technique. To compare the proposed wT_1 mapping with single-slice MOLLI T_1 mapping, three ROIs (size: 11 mm \times 11 mm) were positioned in the liver and back muscle. Additionally, three more ROIs were placed for volunteers with repeated scans to conduct a repeatability analysis.

The proposed sequence was additionally scanned with two different flip angles of the gradient echo readout in one volunteer to evaluate the B_1 sensitivity in vivo: once with the nominal flip angle and once with a reduced flip angle of 6° , simulating a reduced B_1 of 75%. A B_1 map using DREAM⁷⁰ was acquired as reference (breath-hold scan, FOV = 400 \times 400 \times 196.8 mm³, voxel size = 3 \times 3 \times 12 mm³ (2D), $T_E = [2.07, 4.39]$ ms, $T_R = 7.13$ ms, $R = 2$, scan time = 12 s). In addition to the MOLLI and GRASE protocols, which were used for all 10 volunteers, MOLLI T_1 was acquired with in-plane spatial resolution of 3 mm ($T_E = 1.05$ ms, $T_R = 2.24$ ms) to match the in-plane resolution of the proposed method.

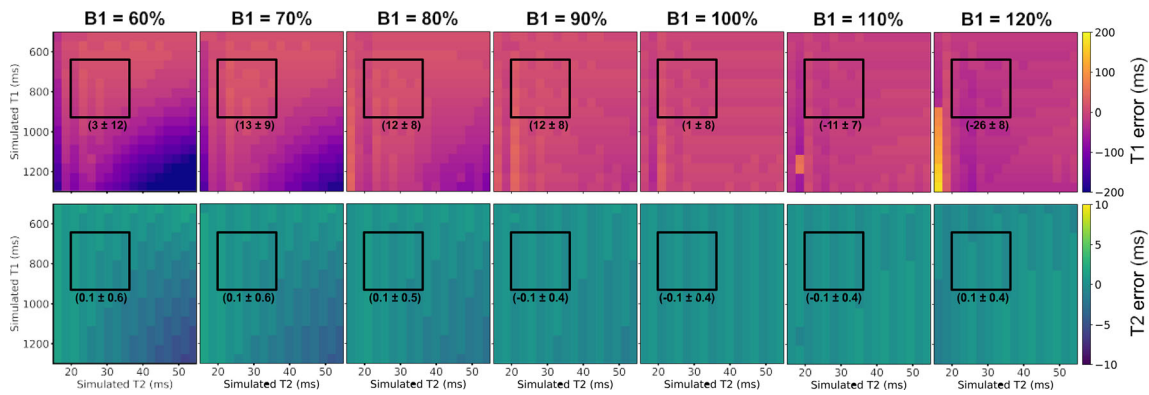


FIGURE 2 Expected errors in T_1 and T_2 measurements resulting from B_1 inhomogeneity, in relation to relaxation parameters. Expected healthy liver relaxation parameters are denoted by a black box annotated with mean and standard deviation of the errors. The figure demonstrates B_1 insensitivity for wT_1 and wT_2 quantification across the entire range of observed B_1 inhomogeneities in the liver.⁷⁷

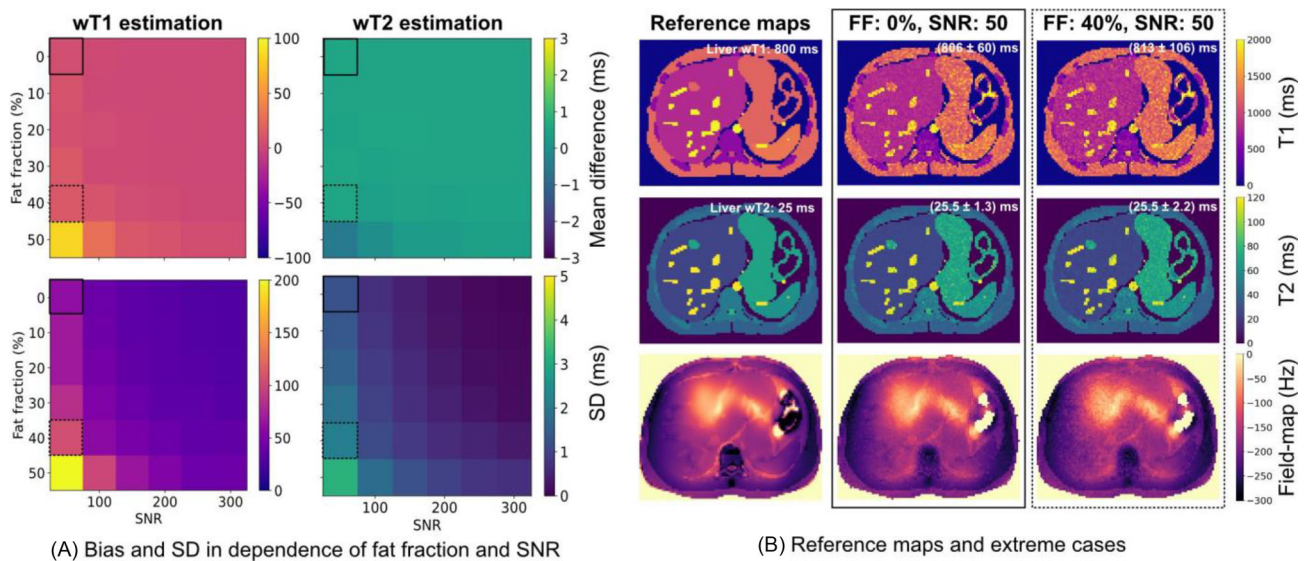


FIGURE 3 SNR and fat fraction simulation in an anatomical body model in the presence of B_0 inhomogeneities. A, Bias (mean difference) and standard deviation (SD) for the whole range of simulated fat fractions and SNR levels. B, Reference wT_1 , wT_2 , and B_0 maps and two extreme cases (FF = 0% and 40%, SNR = 50). Fat does not confound the wT_1 and wT_2 measurements and notable errors only occur at low SNR.

2.3.4 | Patient measurements

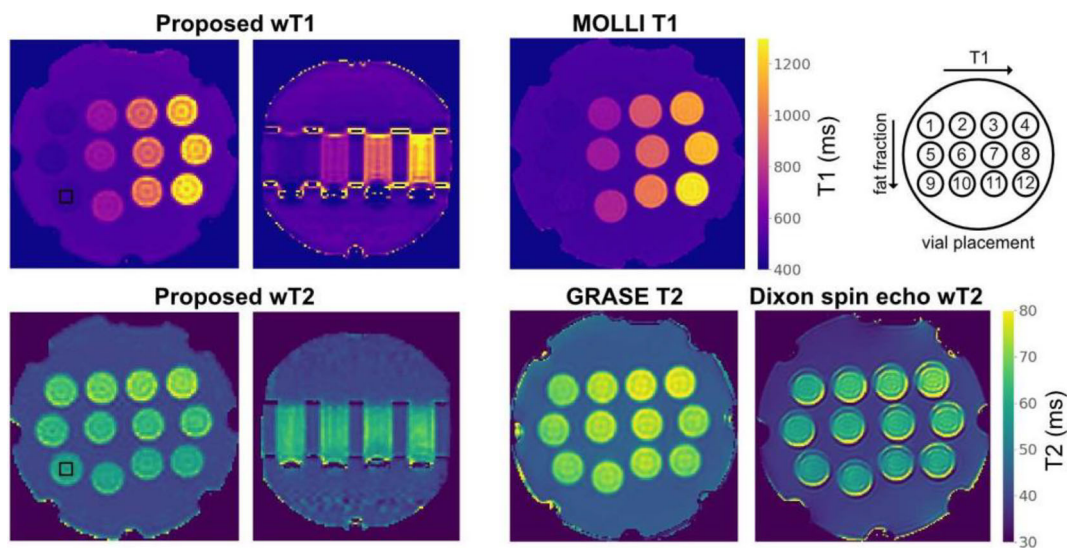
The robustness and clinical usefulness of the proposed technique were evaluated in five liver patients with different abdominal pathologies (compensated liver cirrhosis, fatty liver disease, liver metastasis of pancreatic cancer, and hepatocellular carcinoma). The proposed technique was scanned in addition to the conventional sequences of the clinical protocol used at our institution (Supplementary Table S1). For comparison, an axial T_2 -weighted sequence and a late post-contrast T_1 -weighted fat-suppressed sequence (after injection of a gadolinium-based contrast agent) were chosen to delineate lesions, and a multi-echo gradient echo acquisition was used for PDF mapping.

2.3.5 | Data processing

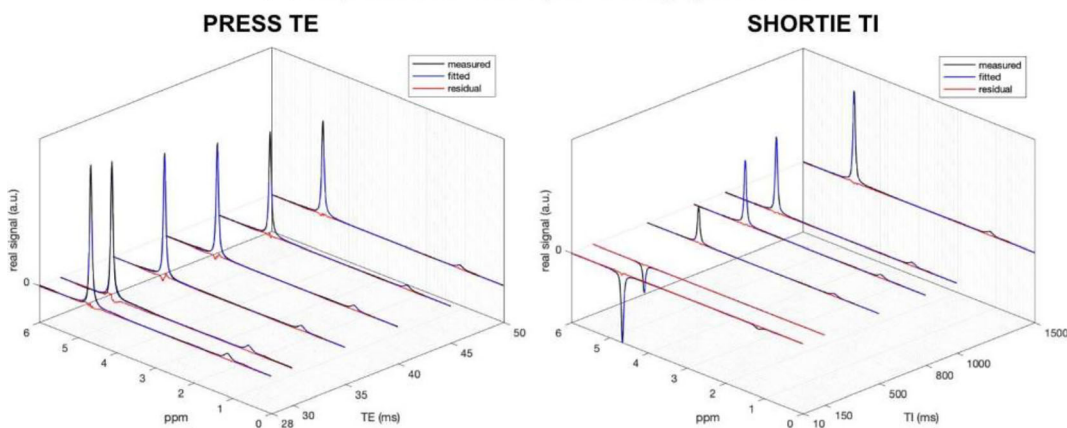
Motion estimation and iterative reconstruction⁷¹ were implemented in Julia 1.9, and Bloch simulations, water-fat separation and dictionary matching in Python 3.10. The non-uniform fast Fourier transform was performed on a GPU (NVIDIA RTX A6000).⁷² Total processing times per data set were (26.5 ± 1.8) min. The source code and phantom data will be made publicly available: <https://github.com/BMRRgroup/liver-t1t2-mapping>.

The regularization parameters $\alpha_1 = 0.03$ and $\alpha_2 = 0.3$ were optimized to reduce streaking artifacts while preserving imaging details. A nine-peak fat model was assumed for simulation and water-fat separation.^{73,74} For visualization, the proposed wT_1 and wT_2 maps were masked based on the fat fraction (<70%) calculated from the T2prep with $T_{\text{prep}} = 10.9$ ms, and were plotted onto the proton density map, which was additionally obtained from dictionary matching.

Other imaging techniques were processed using the scanner's online reconstruction and fitting routines. For Dixon spin echo wT_2 , fat-suppressed images for the different echo times were fitted to a mono-exponential model. Spectroscopy data was processed using the ALFONSO⁷⁵ framework applying coil combination, signal averaging, frequency offset correction, phase correction, and signal fitting. Specifically, model fitting was performed in the time domain and jointly for the T_1/T_E series using the nonlinear least-squares solver NL2SOL.^{58,76} The fat fraction values for the phantom vials were taken from the phantom manufacturer's specifications (T_1 Calimetrix phantom) or were taken from a STEAM T_E spectroscopy scan ($T_E = [10, 15, 20, 25, 75]$ ms, $T_R = 5$ s) using the same MRS processing as described above (custom-built T_2 phantom).



(A) Proposed wT_1/wT_2 maps and imaging reference



(B) Spectroscopy reference for vial 9

FIGURE 4 Comparison of the proposed wT_1 and wT_2 mapping with conventional methods and MRS reference. A, T_1 phantom experiment displaying the proposed simultaneous wT_1 and wT_2 mapping alongside MOLLI T_1 mapping, GRASE T_2 , and Dixon spin echo wT_2 mapping. The black box in the maps indicates the voxel used for the spectroscopy reference presented in B. Voxels of similar size were positioned in all vials for MRS. B, Two MRS spectra from the PRESS and SHORTIE sequences employed for wT_1 and wT_2 estimation. The measured spectra are depicted in black, while the simultaneous T_E/T_1 series fit is shown in blue.

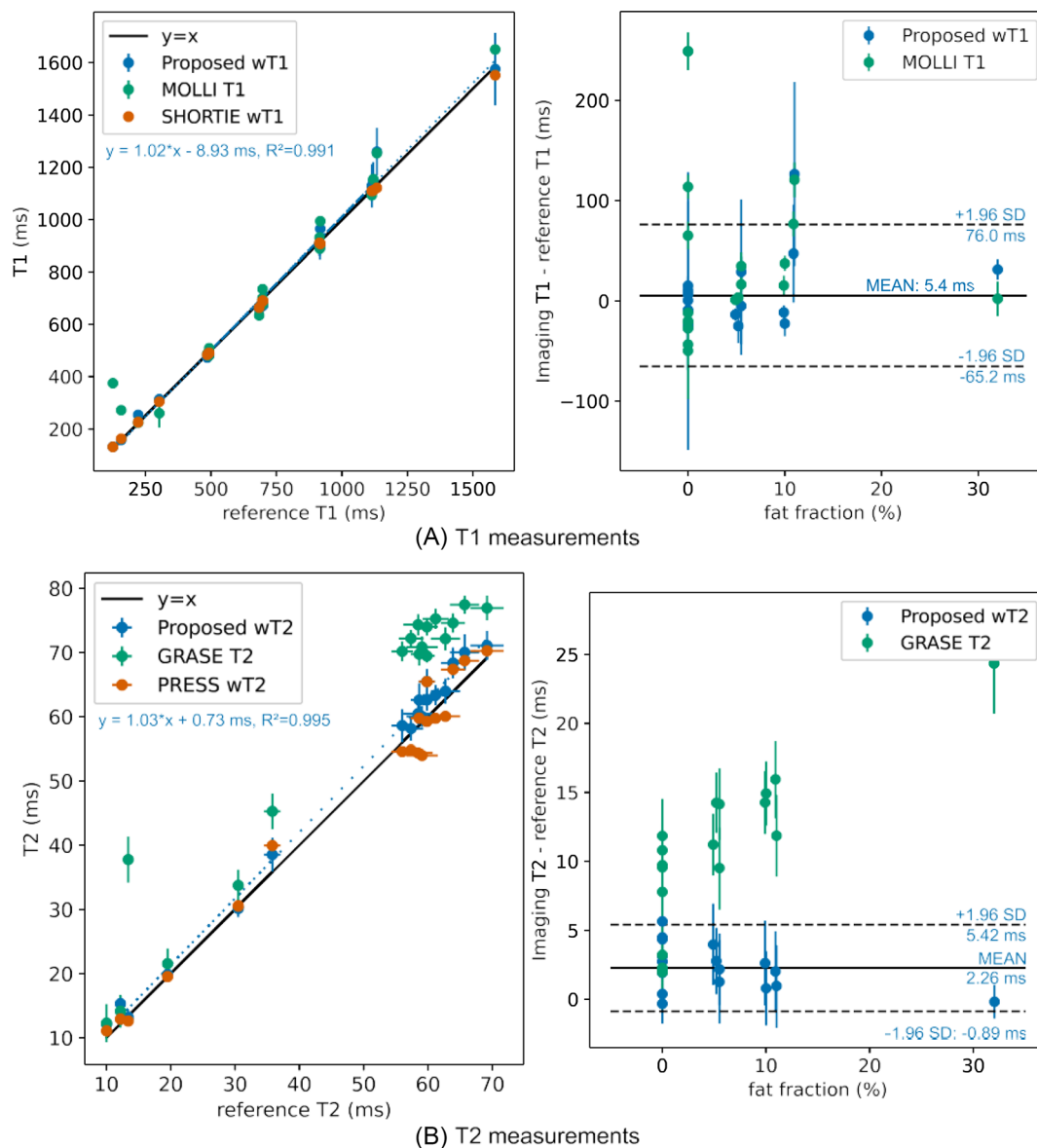


FIGURE 5 Quantitative evaluation of phantom experiments for T_1 measurements (A) and T_2 measurements (B). The reference wT_1 measurement is obtained using a STEAM T_1 series spectroscopy sequence, while the reference T_2 measurement employs a Dixon spin echo imaging sequence. The left plots compare T_1 and T_2 estimates from methods used in the volunteer study with reference values, which are infeasible to acquire in vivo due to their lengthy acquisition times. The right plots show the differences between the proposed method, MOLLI, and GRASE and their respective references (vertical axis) for various fat fractions (horizontal axis). The mean difference (solid line) and standard deviation (SD, dashed line) are presented for the proposed method to estimate bias and precision in comparison to the reference.

3 | RESULTS

3.1 | B_1 , fat fraction, and SNR simulation

Figure 2 illustrates the B_1 sensitivity of the optimized pulse sequence parameters, analyzed through Bloch simulations across various relaxation parameters. The errors between the simulated and estimated T_1 and T_2 relaxation times are minimal for the anticipated healthy liver relaxation parameters within the expected range of B_1 inhomogeneities in the liver at 3T (B_1 between 60% and 115%).⁷⁷ For lower B_1 values, a bias in T_1 estimation increases for long T_1 and T_2 relaxation times.

The body model simulation in Figure 3 shows the bias and precision of the wT_1 and wT_2 estimates for different fat fractions and SNR levels. The parameter estimation is unbiased for the entire range of simulated fat fractions (0–50%) for moderate and higher SNR ($\text{SNR} \geq 50$). At low SNR

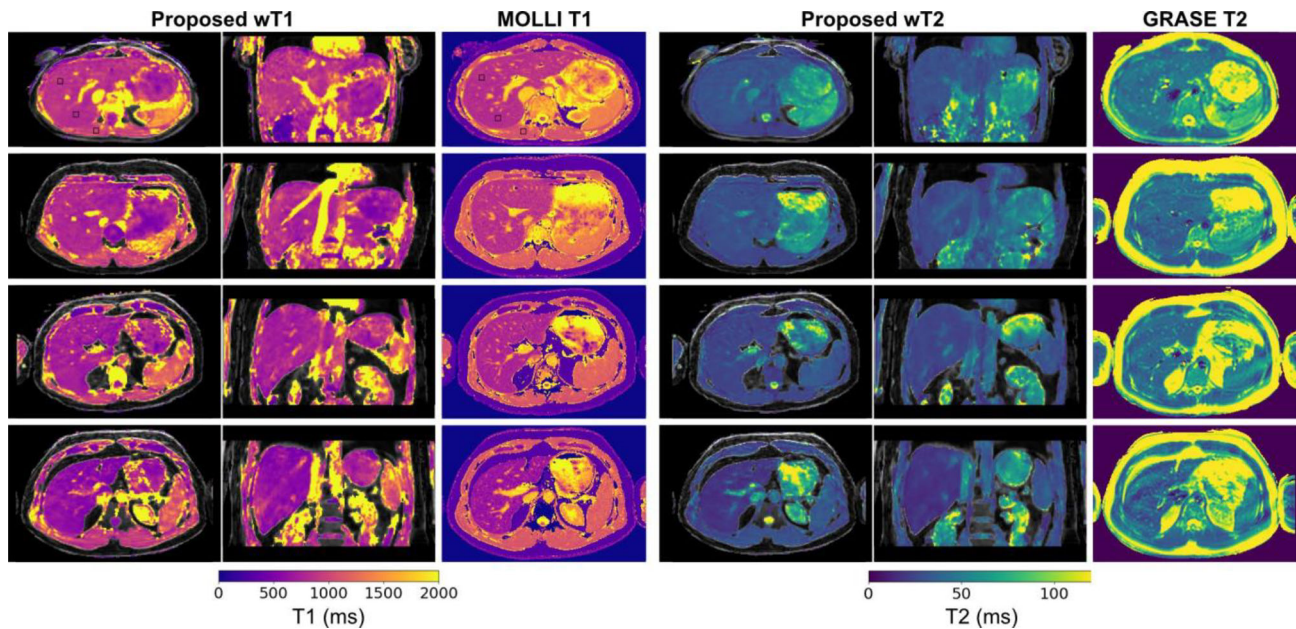


FIGURE 6 Comparison of the proposed wT_1 and wT_2 mapping with MOLLI T_1 and GRASE T_2 mapping for four volunteers (numbers 3, 5, 6, and 9) and a representative slice. Both axial and coronal planes are displayed for the proposed method, as it acquires the entire liver volume, while MOLLI and GRASE are 2D sequences with limited slice coverage. The placement of the ROIs for quantitative evaluation (Figure 7) is representatively shown in the T_1 maps of one volunteer.

(SNR = 50), the standard deviation increases to 60 ms and 1.3 ms for T_1 and T_2 and a fat fraction of 0%. For higher fat fractions and low SNR, the standard deviation increases and for large fat fractions a bias may occur depending on the B_0 inhomogeneities and the quality of the estimation.

3.2 | Phantom results

Figure 4A shows the proposed, MOLLI, GRASE, and Dixon spin echo maps in the T_1 Calimetric phantom. Coronal reformats, only possible for the proposed method as it is a 3D sequence, demonstrate good homogeneity throughout the entire FOV. For the GRASE T_2 map, noticeably higher T_2 values, compared with the proposed wT_2 mapping and Dixon spin echo, can be visually identified. Supplementary Figure S2 shows the proposed and reference maps in the custom-built T_2 phantom.

The quantitative evaluation in Figure 5 indicates an excellent agreement between the proposed wT_1 mapping and STEAM T_1 (mean difference: (5 ± 36) ms) and between the two MRS techniques, SHORTIE T_1 and STEAM T_1 (mean difference: (-6 ± 9) ms). The standard deviation for the proposed wT_1 increases for higher T_1 values, related to the ringing that can be observed in the phantom. MOLLI T_1 deviates from the spectroscopy reference for vials with shorter T_2 values and slightly overestimates for those with longer T_2 values and higher fat fractions, with an overall mean difference of (31 ± 71) ms. The proposed method exhibits a good agreement with Dixon spin echo, with a mean difference of (2.3 ± 1.6) ms. The PRESS MRS technique, used as the T_2 reference for the in vivo experiments, generally corresponds well to Dixon spin echo (mean difference: (0.1 ± 2.7) ms) but shows a larger difference than the proposed method for the bottom row of the T_1 Calimetric phantom. GRASE T_2 has a mean difference of (10.5 ± 5.6) ms with regard to Dixon spin echo and shows increasing differences from the reference with increasing fat fraction. A quantification bias related to the fat fraction cannot be determined for the proposed wT_1 and wT_2 mapping. The proposed method and comparison results for all ROIs are listed in Supplementary Tables S2 and S3.

Supplementary Figure S4 shows that dictionary matching without prior fat suppression leads to significant quantification errors. Moreover, the combined dictionary matching of T_1 prep and T_2 prep proves to be important for parameter accuracy (Supplementary Figure S5).

3.3 | In vivo volunteer results

Figure 6 provides a summary of in vivo maps for four volunteers. The superior in-plane spatial resolution of single-slice MOLLI is evident, while the proposed method enables whole-liver coverage. GRASE liver T_2 maps are shown to be more inhomogeneous and more susceptible to artifacts than the proposed wT_2 maps.

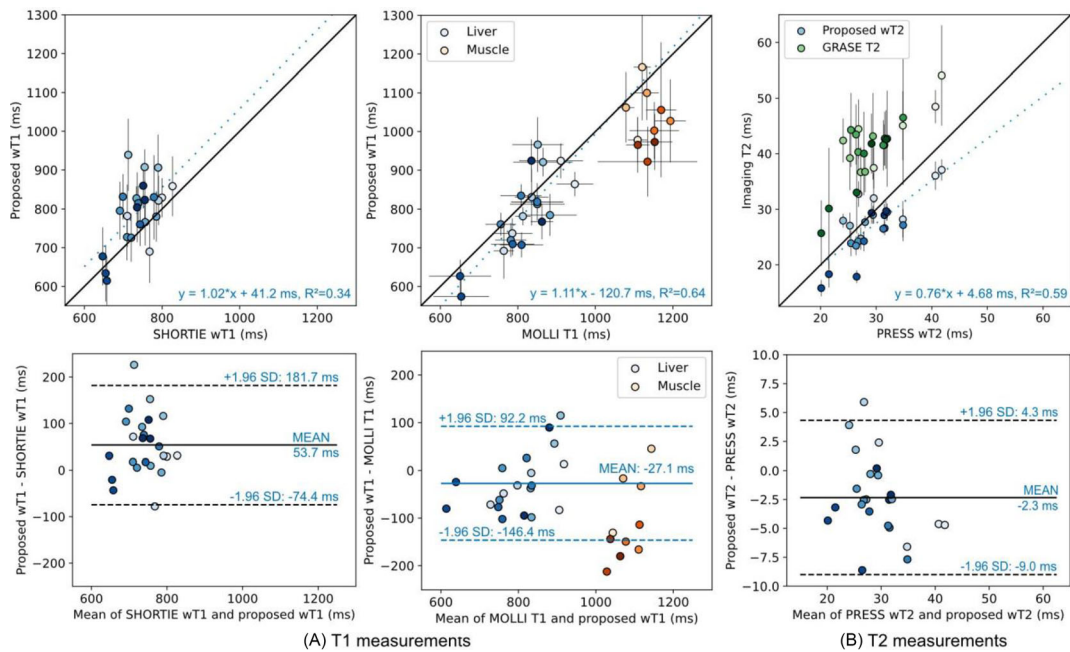


FIGURE 7 Quantitative evaluation of the volunteer study for T_1 measurements (A) and T_2 measurements (B). In the upper part of the figure, the scatter plots show the linear correlation of the proposed method with reference sequences, while the lower plots present Bland-Altman analyses. The color shading denotes the volunteer number. The first column compares the proposed wT_1 with SHORTIE wT_1 , showing higher wT_1 for the proposed method. Three ROIs per subject were scanned. In total, six ROIs with standard deviations larger than 110 ms were excluded due to the included blood vessels confounding the quantification. The middle column compares the proposed wT_1 with MOLLI for three ROIs in the liver and muscle, showing a good correlation, with slightly lower estimated wT_1 for the proposed wT_1 compared with MOLLI T_1 . The T_2 evaluation (third column) indicates better agreement between the proposed method and PRESS than with GRASE. Additionally, GRASE exhibits notably higher standard deviations in the ROIs compared with the proposed wT_2 mapping.

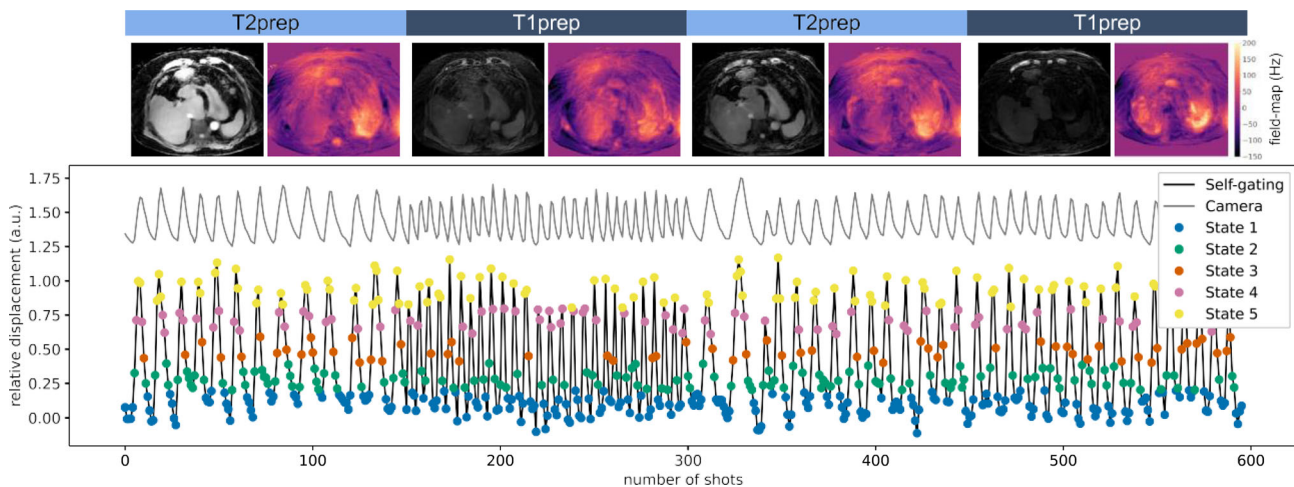


FIGURE 8 Self-gated respiratory motion signal for Patient 1 based on Equation (3) showing the relative displacement of the liver throughout the scan. Motion states were determined based on the amplitude of the motion signal. The respiratory motion signal from the vendor-provided auxiliary camera^{60–63} is displayed as a reference in gray. At the top, the different preparations during the free-breathing acquisition are highlighted. The fat-suppressed images and the field-map of the first motion state (end-expiration) obtained from the water-fat separation are presented for each preparation.

A quantitative evaluation of the proposed wT_1 and wT_2 mapping for all volunteers is presented in Figure 7, and Supplementary Tables S4 and S5. In general, results similar to those in the phantom are found, with an agreement of the proposed method with the MRS reference measurements ($wT_1 = 1.02wT_{1,ref} + 41.2\text{ms}$, $R^2 = 0.34$). In contrast to the results in the phantom, the proposed method, SHORTIE T_1 , and MOLLI show greater divergence among themselves. The mean difference between MOLLI T_1 and the proposed wT_1 in the liver is (-27 ± 61) ms, showing a

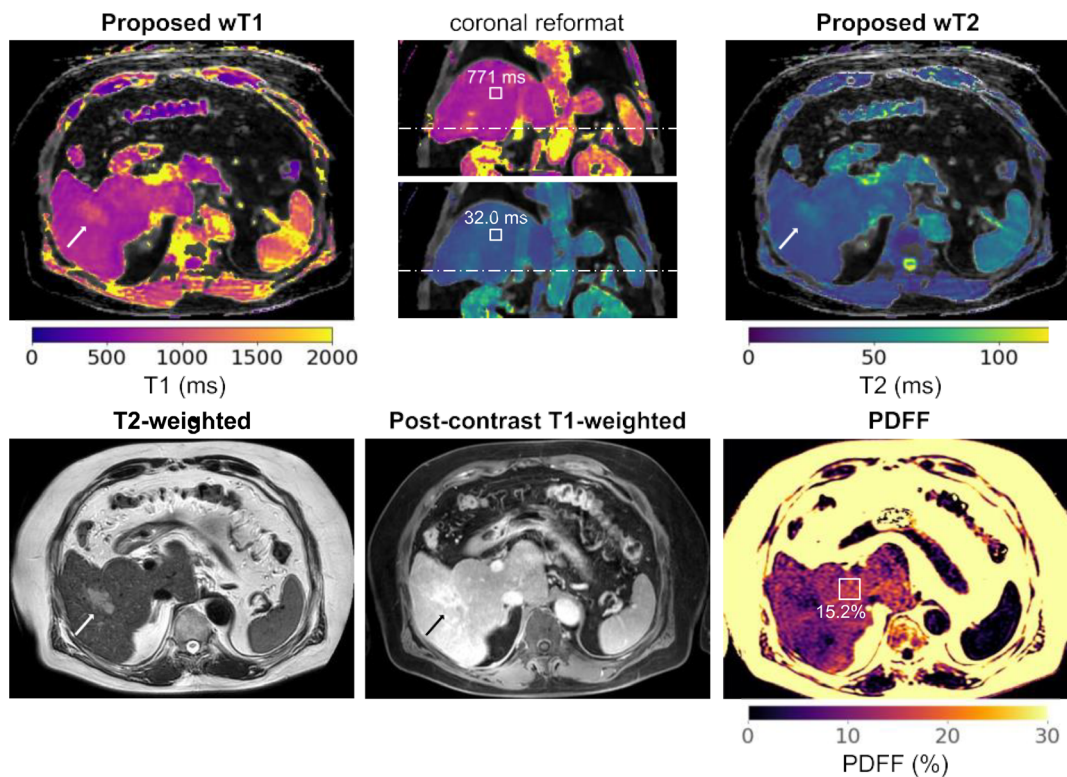


FIGURE 9 Proposed liver wT_1 and wT_2 mapping in Patient 1 with hepatocellular carcinoma and elevated liver fat fraction (approximately 15%). Clinically utilized T_2 -weighted sequences, a post-contrast T_1 -weighted sequence, and the PDFF map are provided as references. The lesion visible in the T_2 -weighted and post-contrast T_1 -weighted scans (indicated by the arrow) can be identified in the proposed wT_1 and wT_2 maps. The slice position is illustrated by the dashed line in the coronal reformat of the wT_1 and wT_2 maps. Mean liver wT_1 and wT_2 values are displayed for an ROI in the coronal reformat.

slightly larger deviation for higher T_1 values in muscle. The proposed wT_2 mapping demonstrates good agreement with PRESS MRS, albeit with slightly lower values (average difference: (-2.3 ± 3.4) ms), while GRASE considerably overestimates PRESS and the proposed wT_2 .

Supplementary Figure S6 shows the repeatability analysis in a subset of the volunteer study. A good agreement with average difference $\Delta wT_2 = (0.2 \pm 1.3)$ ms and $\Delta wT_1 = (-19 \pm 43)$ ms was found.

Furthermore, the effects of confounding factors on the image quality were investigated. The effect of the T_1 blurring correction is assessed in vivo in Supplementary Figure S7, showing slight improvements due to the T_1 blurring correction in the visualization of vessels. Supplementary Figure S8 evaluates the B_1 sensitivity in vivo, showing strong B_1 inhomogeneities in the range from 60% to 120% but comparable image quality for the proposed method with two different flip angles, even if additional B_1 inhomogeneities are simulated. The robustness of the proposed sequence with regard to respiratory motion is another important property. Supplementary Figure S9 shows the self-navigator signal for different volunteers with varying breathing patterns. Supplementary Figure S10 compares the proposed motion-resolved reconstruction with a motion-averaged reconstruction and shows improvements in the visualization of vessels and in quantification using the motion-resolved reconstruction, especially in the upper part of the liver. Supplementary Figure S11 shows wT_1 and wT_2 maps for each of the five motion states. In addition, Supplementary Figure S12 compares the proposed wT_1 and wT_2 maps with MOLLI T_1 and GRASE T_2 at the same nominal in-plane resolution to visualize any loss in texture details due to confounding factors such as T_1 blurring or motion. The appearance of the vessels is slightly different in the proposed wT_1 maps.

3.4 | In vivo patient results

The proposed wT_1 and wT_2 mapping was successively carried out in all five patients (Supplementary Figure S13). Figure 8 displays the self-gating signal of one of the patient scans and compares the extracted motion signal with a surrogate respiratory signal based on the vendor's provided auxiliary camera.

Figure 9 demonstrates the results in a 73-year-old patient with hepatocellular carcinoma in segment VI adjacent to a portal vein branch with macrovascular invasion. The proposed wT_1 and wT_2 mapping can identify the lesion ($wT_{1, \text{lesion}} = (1028 \pm 41)$ ms and $wT_{2, \text{lesion}} = (42.8 \pm 3.2)$ ms), which can also be delineated in a T_2 -weighted and post-contrast scan of a clinical liver examination. Homogeneous wT_1 and wT_2 maps

($wT_{1,\text{healthy tissue}} = (771 \pm 21.4)$ ms and $wT_{2,\text{healthy tissue}} = (32.0 \pm 1.1)$ ms) are estimated even though the liver fat fraction is significantly increased, by at least 15%, and spatially heterogeneous.

Supplementary Figure S14 presents the results in a 68-year-old patient with decompensated liver cirrhosis and resistant ascites.

4 | DISCUSSION

The present work introduces a method for free-breathing self-navigated whole-liver wT_1 and wT_2 mapping. The proposed method allows simultaneous quantification of wT_1 and wT_2 while being B_1 insensitive for liver relaxation times at 3 T by using an adiabatic modified BIR-4 preparation pulse and optimized sequence parameters. The novel data acquisition scheme was combined with a motion-resolved reconstruction and parameter quantification based on dictionary matching.

The first important feature of the proposed technique is its performance in terms of accuracy and precision. Results demonstrated the ability of the proposed method to estimate simultaneously wT_1 and wT_2 maps of the whole liver at an isotropic resolution of 3 mm in around 6 min. The robust fat suppression performance of the proposed method was investigated in a simulation of an anatomical body model as a function of SNR. However, the Dixon readout with two echoes is not suitable for quantitative PDFF mapping, as confounding effects such as R_2^* are not sufficiently corrected in comparison with clinical PDFF mapping with more acquired echoes.⁸ wT_1 and wT_2 maps were robustly estimated in all 10 volunteers and five patients. The proposed method showed good T_1 and T_2 quantification accuracy in the phantom, with an increase in standard deviation for higher T_1 values. In vivo results generally agreed with phantom findings and highlighted the biased and imprecise quantification of GRASE T_2 mapping that is to be expected, for example, due to stimulated echo pathways.⁷⁸ The proposed method yielded slightly lower values in vivo than MOLLI in subjects with no relevant liver fat content. The deviation of the proposed wT_1 and MOLLI T_1 increased at longer T_1 values, as in the muscle. It is known that MOLLI quantification can be biased depending on experimental conditions,^{79,80} as can be seen for the custom-built T_2 phantom with a bias for vials with small T_2 values or a slight overestimation associated with the fat fraction for the T_1 phantom. In addition, the proposed method might be affected by Gibbs ringing, T_1 blurring, and B_1 sensitivity at longer T_1 values, as validated in simulations and phantom experiments. The proposed method showed the best agreement with spectroscopy in vivo when compared with other imaging techniques, with a small overestimation for T_1 compared with SHORTIE T_1 and a slight underestimation for T_2 compared with PRESS T_E . Neither spectroscopy technique can be regarded as a perfect reference, as both techniques have been optimized to be performed in a single breath-hold. Effects such as blood flow and residual motion can lead to differences between the phantom and in vivo measurements. The proposed method demonstrated excellent repeatability for wT_2 and a slight bias of 20 ms for wT_1 .

A second important feature of the proposed technique is its free-breathing acquisition mode. Various T_1 and T_2 mapping methods have been proposed relying on single breath-holds, with the advantage of short acquisition times.^{29,34,81,82} However, many breath-hold-based methods only measure a specific number of slices without covering the entire liver. Moreover, breath-hold scans may not be feasible for sick patients. In contrast, free-breathing scans have a longer acquisition time but offer the advantage of a 3D acquisition of the entire liver with better resolution along the F/H axis, allowing for a more comprehensive assessment of changes throughout the liver.

While other proposed whole-liver free-breathing T_1 mapping techniques typically rely on a Look-Locker scheme acquiring multiple different inversion contrasts after a single inversion pulse,^{32,33,42} the proposed technique acquires only a single image volume after the inversion pulse. Although the proposed approach limits the dynamic range and the contrast of the T_1 preparations, T_1 mapping can be successfully performed due to the applied dictionary matching approach. Moreover, in contrast to the use of a Look-Locker scheme, the proposed acquisition is capable of leveraging several advantages of the radial stack-of-stars trajectory.³²

First, acquiring only a single inversion contrast per preparation allows for greater flexibility in selecting the F/H resolution, enabling an isotropic resolution of 3 mm for the proposed method, whereas other Look-Locker methods apply an F/H resolution of the order of 6 or 5 mm. Although these other Look-Locker methods have an increased in-plane resolution, the proposed method can also achieve a finer in-plane resolution by increasing the number of acquired radial spokes. A preliminary work on free-breathing whole-liver wT_1 and wT_2 mapping at 1.5 T has demonstrated the possibility of increasing the F/H resolution using a variable density Cartesian trajectory.⁴⁰ However, similar to other methods, T_1 relaxation along the readout introduces blurring along the F/H axis, which can limit the actual resolution along the axis. In this work, we reweighted k -space based on correction factors computed from Bloch simulations with different relaxation parameters. The proposed T_1 blurring correction reduces blurring but cannot completely correct relaxation blurring, as the blurring differs for each tissue depending on its T_1 and T_2 . In addition, TV-regularized image reconstruction may sacrifice small details in order to reduce streaking artifacts. This trade-off between minimizing undersampling artifacts and preserving small features may affect the spatial resolution of the reconstructed images. The actual spatial resolution in the F/H direction is probably lower than the acquisition resolution due to motion and T_1 blurring effects. The actual in-plane spatial resolution might be similarly affected by motion due to residual motion blurring within the five motion states, with effects on image quality varying by subject.

Second, the acquisition of only a single inversion contrast per preparation additionally reduces the contrast variation across k_z projections. This ensures the possibility of using the self-navigating properties of the stack-of-stars trajectory, whereas the time-interleaved acquisition of

multiple different contrasts after a single inversion results in varying contrasts along the k_z projections and may complicate self-navigation.³² The proposed method applies a PCA-based motion estimation of the oversampled k -space center with rescaling for each dynamic. Other free-breathing relaxometry works require the acquisition of MR navigators,⁴⁰ navigator-like training data (which is also beneficial for the implemented tensor-based image reconstruction),³³ or the use of an external surrogate respiratory motion signal, such as a respiratory bellow.³² The use of additional navigator pulses prolongs the total acquisition time and navigators need to be carefully designed to not interfere with the imaging process. The respiratory bellow depends on proper placement and therefore may not be as reliable as an MR navigator.⁸³ Instead, the motion estimation and motion-resolved reconstruction performed robustly in both the volunteer and patient study.

Two of the most prominent methods proposed for liver relaxometry are MR fingerprinting (MRF)^{81,84} and MR multitasking.^{33,41} The proposed method incorporates some of their concepts and also has unique features. Previous liver MRF methods use low flip angles and various inversion and T2prep pulses to acquire multiple quantitative maps while being B_1 insensitive, e.g., water-specific T_1 , T_2 , $T_{1\rho}$ and T_2^* and PDFF.⁸⁴ The proposed method also uses an adiabatic preparation pulse, but the acquisition parameters are not continuously varied during data acquisition as in MRF.⁸⁵ Instead, the proposed method includes the optimization of the sequence parameters to minimize B_1 sensitivity over the four acquired relaxometry contrasts. MRF in the liver has mostly been investigated as single-slice radial acquisition in a breath-hold,^{81,84} whereas the proposed method acquires volumetric whole-liver maps during free-breathing. To enable simultaneous wT_1 and wT_2 mapping from only four acquired relaxometry contrasts, dictionary matching similar to MRF was used in the proposed method. The dictionary enables the direct integration of confounding factors such as B_0 inhomogeneity. Liver multitasking uses a Look-Locker scheme and a radial stack-of-stars trajectory acquiring wT_1 , R_2^* , and PDFF while assuming an analytical signal model. Previous multitasking methods acquire maps with $1.5 \times 1.5 \times 6\text{mm}^3$ resolution in 5 or 7 min during free-breathing, depending on whether two different flip angles are acquired for B_1 correction.⁴¹ In multitasking, a k -space line along the k_z axis is acquired every eight readouts for motion navigation (every 74 ms), while the proposed method uses a self-navigator acquired over the entire readout (about 245 ms). The centric profile ordering along k_z of the proposed method compared with the Gaussian-density randomized ordering for multitasking could improve the motion robustness, whereas the randomized ordering improves incoherence and allows higher undersampling strengths. An important difference between the proposed method and multitasking is the acquisition of fewer inversion contrasts and the acquisition of an additional wT_2 map instead of PDFF and R_2^* maps. However, MR multitasking has also been combined with T2preps for the acquisition of T_2 maps in other anatomies with different acquisitions, e.g., 2D T_1 and T_2 mapping in cardiac imaging.⁸⁶ In multitasking, a large number of different images are acquired with strong undersampling and different inversion contrast, exploiting low-rank properties of the data during image reconstruction. The proposed method does not rely on a low-rank reconstruction, although this could further enhance the image quality.

The proposed co-registered wT_1 and wT_2 maps can become clinically relevant, as studies have shown the benefits of both T_1 and T_2 mapping in the liver and its combination.^{15,87} The presented patient cases demonstrate the ability of the proposed method to depict liver lesions in a liver cancer patient with increased liver fat content. The water-fat separation is of great importance for T_1 and T_2 quantification, as shown in the phantom experiment without fat suppression, leading to a significant quantification bias (Supplementary Figure S4). The proposed method is expected to be applicable in patients with liver iron overload and short T_2 and T_2^* , as the T_2 quantification performance was robust even in the phantom with short T_2 values. The combined dictionary matching approach also accounts for possible confounding effects in the T_1 estimate. The water-fat separation performance might be affected since R_2^* is not modeled in the signal model, although the effect is minimized by the two echoes with short echo times. In the case of diffuse liver disease, spatial resolution may be slightly reduced (i.e., for detecting and staging of fibroinflammation⁸⁸), allowing further reduction in acquisition time. It should be noted that changing the F/H resolution in particular changes the readout and optimization of a subset of the acquisition parameters could be beneficial. In addition, the minimum shot duration T_{shot} cannot be reduced to a minimum due to the SAR limitations of the BIR-4 preparation pulse.

The present work has some limitations. First, the achieved T1prep contrast is reduced in regions with strong B_0 inhomogeneities, such as the upper part of the liver, which increases the uncertainty of parameter estimation. Sequence timings were optimized to minimize B_1 sensitivity for T_1 and T_2 mapping, and the proposed method used a B_0 -specific dictionary to correct for B_0 inhomogeneities during parameter fitting. To further improve parameter estimation in the upper liver area, a combined optimization of sequence parameters with respect to B_1 and B_0 sensitivity might be beneficial. Second, the proposed technique shows good B_1 insensitivity in a simulation for the expected liver parameters in a B_1 range of 60–120% with remaining B_1 sensitivity at longer T_1 and T_2 values. In the case of very severe B_1 inhomogeneities, quantification bias may occur. Adding an additional T1prep might reduce the B_1 sensitivity but would increase scan time. Third, the proposed method acquires only a single inversion contrast after the inversion pulse. The amount of sampled contrast information along the T_1 recovery may be limited compared with a classical Look-Locker method, but offers several advantages—for example, the flexibility in combination with T2preps or the choice of spatial resolution. To obtain additional data about the T_1 recovery, additional T1preps must be added, which increases the scan time. Fourth, a simultaneous mapping of wT_1 , wT_2 , R_2^* , and PDFF would be interesting to correct for R_2^* as a possible confounding factor and to better understand the interplay of liver inflammation, fibrosis, iron content, and fat content. There are free-breathing techniques that perform wT_1 mapping along with R_2^* and PDFF,³³ but they do not include wT_2 mapping. The current sequence could be modified to acquire more echoes for the additional mapping of R_2^* and PDFF. Fifth, applying a deep-learning-based regularizer could reduce computation time, eliminate the need to fine-tune regularization terms, and potentially enable the reconstruction of parameter maps with finer details that might be smoothed due to current TV

regularization.^{89,90} In contrast to 2D data or other anatomies, the difficulty in applying deep learning to the reconstruction of the present data is, in addition to GPU memory, that fully sampled motion-free ground truth images are not available for training, as increasing the acquisition time would likely result in more subject motion. Sixth, the 1D self-navigation signal corresponds well to the signal from the vendor-provided respiratory motion camera, but a higher dimensional MR navigator could extract more information for motion compensation,⁹¹ although changes to the pulse sequence would be necessary. In addition, multiple preparations were acquired sequentially during a 6 min scan, and subject motion may occur during the scan. Registration of the different preparation volumes could reduce the influence of subject motion on the quality of the wT_1 and wT_2 maps.

5 | CONCLUSION

In this work, a method for free-breathing whole-liver simultaneous wT_1 and wT_2 mapping was proposed. The method consists of a novel pulse sequence combined with a motion-resolved reconstruction and dictionary mapping-based parameter estimation. The proposed method enables the simultaneous and co-registered mapping of wT_1 and wT_2 at 3T in the presence of B_1 and B_0 inhomogeneities, and allows whole-liver wT_1 and wT_2 mapping with high accuracy at an isotropic nominal spatial resolution of 3 mm in a fixed acquisition time of 6 min during free breathing.

ACKNOWLEDGEMENTS

The present work was supported by the TUM International Graduate School of Science and Engineering (TUM-ICL Joint Academy of Doctoral Studies). The authors also acknowledge research support from Philips Healthcare. The authors would also like to thank Dr Stefan Ruschke for developing the SHORTIE MRS sequence and processing, Dr Christof Böhm for helpful discussions regarding the field-mapping algorithm, Dr Jakob Meineke for helpful discussions regarding the motion compensation aspects, and Dr Florian Knoll for helpful discussions regarding the partial Fourier reconstruction. Open access funding enabled and organized by Projekt DEAL.

CONFLICT OF INTEREST STATEMENT

Kilian Weiss is an employee of Philips GmbH Market DACH; Dimitrios Karampinos receives grant support from Philips Healthcare.

ORCID

Jonathan Stelter  <https://orcid.org/0000-0003-3335-3331>

REFERENCES

1. Younossi Z, Anstee QM, Marietti M, et al. Global burden of NAFLD and NASH: trends, predictions, risk factors and prevention. *Nat Rev Gastroenterol Hepatol*. 2017;15(1):11-20. doi:10.1038/nrgastro.2017.109
2. Younossi Z, Tacke F, Arrese M, et al. Global perspectives on nonalcoholic fatty liver disease and nonalcoholic steatohepatitis. *Hepatology*. 2019;69(6):2672-2682. doi:10.1002/hep.30251
3. Rinella ME, Lazarus JV, Ratziu V, et al. A multi-society Delphi consensus statement on new fatty liver disease nomenclature. *J Hepatol*. 2023;79(6):1542-1556. doi:10.1016/j.jhep.2023.06.003
4. Anstee QM, Targher G, Day CP. Progression of NAFLD to diabetes mellitus, cardiovascular disease or cirrhosis. *Nat Rev Gastroenterol Hepatol*. 2013;10(6):330-344. doi:10.1038/nrgastro.2013.41
5. Banerjee R, Pavlides M, Tunnicliffe EM, et al. Multiparametric magnetic resonance for the non-invasive diagnosis of liver disease. *J Hepatol*. 2014;60(1):69-77. doi:10.1016/j.jhep.2013.09.002
6. Pavlides M, Banerjee R, Tunnicliffe EM, et al. Multiparametric magnetic resonance imaging for the assessment of non-alcoholic fatty liver disease severity. *Liver Int*. 2017;37(7):1065-1073. doi:10.1111/liv.13284
7. Reeder SB, Cruite I, Hamilton G, Sirlin CB. Quantitative assessment of liver fat with magnetic resonance imaging and spectroscopy. *J Magn Reson Imaging*. 2011;34(4):729-749. doi:10.1002/jmri.22580
8. Reeder SB, Hu HH, Sirlin CB. Proton density fat-fraction: a standardized MR-based biomarker of tissue fat concentration. *J Magn Reson Imaging*. 2012;36(5):1011-1014. doi:10.1002/jmri.23741
9. Hernandez D, Levin YS, Sirlin CB, Reeder SB. Quantification of liver iron with MRI: state of the art and remaining challenges. *J Magn Reson Imaging*. 2014;40(5):1003-1021. doi:10.1002/jmri.24584
10. Wood JC, Enriquez C, Ghugre N, et al. MRI R2 and R2* mapping accurately estimates hepatic iron concentration in transfusion-dependent thalassemia and sickle cell disease patients. *Blood*. 2005;106(4):1460-1465. doi:10.1182/blood-2004-10-3982
11. Venkatesh SK, Yin M, Ehman RL. Magnetic resonance elastography of liver: technique, analysis, and clinical applications. *J Magn Reson Imaging*. 2013;37(3):544-555. doi:10.1002/jmri.23731
12. Hoad CL, Palaniyappan N, Kaye P, et al. A study of t1 relaxation time as a measure of liver fibrosis and the influence of confounding histological factors. *NMR Biomed*. 2015;28(6):706-714. doi:10.1002/nbm.3299
13. Guimaraes AR, Siqueira L, Uppal R, et al. T2 relaxation time is related to liver fibrosis severity. *Quant Imaging Med Surg*. 2016;6(2):103-114. doi:10.21037/qims.2016.03.02
14. Luetkens JA, Klein S, Träber F, et al. Quantification of liver fibrosis at T1 and T2 mapping with extracellular volume fraction MRI: preclinical results. *Radiology*. 2018;288(3):748-754. doi:10.1148/radiol.2018180051

15. Hoffman DH, Ayoola A, Nickel D, Han F, Chandarana H, Shanbhogue KP. T1 mapping, T2 mapping and MR elastography of the liver for detection and staging of liver fibrosis. *Abdom Radiol*. 2019;45(3):692-700. doi:10.1007/s00261-019-02382-9
16. O'Brien AT, Gil KE, Varghese J, Simonetti OP, Zareba KM. T2 mapping in myocardial disease: a comprehensive review. *J Cardiovasc Magn Reson*. 2022; 24(1):33. doi:10.1186/s12968-022-00866-0
17. Messroghli DR, Moon JC, Ferreira VM, et al. Clinical recommendations for cardiovascular magnetic resonance mapping of T1, T2, T2* and extracellular volume: a consensus statement by the Society for Cardiovascular Magnetic Resonance (SCMR) endorsed by the European Association for Cardiovascular Imaging (EACVI). *J Cardiovasc Magn Reson*. 2017;19(1):75. doi:10.1186/s12968-017-0389-8
18. Hollingsworth KG, de Sousa PL, Straub V, Carlier PG. Towards harmonization of protocols for MRI outcome measures in skeletal muscle studies: consensus recommendations from two TREAT-NMD NMR workshops, 2 May 2010, Stockholm, Sweden, 1–2 October 2009, Paris, France. *Neuromuscul Disord*. 2012;22:S54-S67. doi:10.1016/j.nmd.2012.06.005
19. Cieszanowski A, Anysz-Grodzicka A, Szeszkowski W, et al. Characterization of focal liver lesions using quantitative techniques: comparison of apparent diffusion coefficient values and T2 relaxation times. *Eur Radiol*. 2012;22(11):2514-2524. doi:10.1007/s00330-012-2519-x
20. Yang W, Kim JE, Choi HC, et al. T2 mapping in gadoteric acid-enhanced MRI: utility for predicting decompensation and death in cirrhosis. *Eur Radiol*. 2021;31(11):8376-8387. doi:10.1007/s00330-021-07805-0
21. Takayama Y, Nishie A, Ishimatsu K, et al. Diagnostic potential of t1rho and t2 relaxations in assessing the severity of liver fibrosis and necro-inflammation. *Magn Reson Imaging*. 2022;87:104-112. doi:10.1016/j.mri.2022.01.002
22. Meloni A, Carnevale A, Gaio P, et al. Liver T1 and T2 mapping in a large cohort of healthy subjects: normal ranges and correlation with age and sex. *Magn Reson Mater Phys Biol Med*. 2024;37:93-100. doi:10.1007/s10334-023-01135-6
23. Rong J, Zhu Y, Zhu K, et al. Utility of T1 mapping and T2 mapping for non-invasive assessment of liver fibrosis: preclinical results. bioRxiv. Preprint posted online November 13, 2023. doi:10.1101/2023.11.08.566354
24. Messroghli DR, Radjenovic A, Kozierke S, Higgins DM, Sivananthan MU, Ridgway JP. Modified Look-Locker inversion recovery (MOLLI) for high-resolution T1 mapping of the heart. *Magn Reson Med*. 2004;52(1):141-146. doi:10.1002/mrm.20110
25. Mozes FE, Tunnicliffe EM, Pavlides M, Robson MD. Influence of fat on liver T1 measurements using modified Look-Locker inversion recovery (MOLLI) methods at 3T. *J Magn Reson Imaging*. 2016;44(1):105-111. doi:10.1002/jmri.25146
26. Li Z, Sun J, Hu X, et al. Assessment of liver fibrosis by variable flip angle T1 mapping at 3.0T. *J Magn Reson Imaging*. 2015;43(3):698-703. doi:10.1002/jmri.25030z
27. Tamada D, Wakayama T, Onishi H, Motosugi U. Multiparameter estimation using multi-echo spoiled gradient echo with variable flip angles and multi-contrast compressed sensing. *Magn Reson Med*. 2018;80(4):1546-1555. doi:10.1002/mrm.27151
28. Tadimalla S, Wilson DJ, Shelley D, et al. Bias, repeatability and reproducibility of liver T1 mapping with variable flip angles. *J Magn Reson Imaging*. 2022;56(4):1042-1052. doi:10.1002/jmri.28127
29. Roberts NT, Tamada D, Muslu Y, Hernando D, Reeder SB. Confounder-corrected T1 mapping in the liver through simultaneous estimation of T1, PDFF, R2*, and B1+ in a single breath-hold acquisition. *Magn Reson Med*. 2023;89(6):2186-2203. doi:10.1002/mrm.29590
30. Belsley G, Tyler DJ, Robson MD, Tunnicliffe EM. Optimal flip angles for in vivo liver 3D T1 mapping and B1+ mapping at 3T. *Magn Reson Med*. 2023; 90(3):950-962. doi:10.1002/mrm.29683
31. Treier R, Steingotter A, Fried M, Schwizer W, Boesiger P. Optimized and combined T1 and B1 mapping technique for fast and accurate T1 quantification in contrast-enhanced abdominal MRI. *Magn Reson Med*. 2007;57(3):568-576. doi:10.1002/mrm.21177
32. Feng L, Liu F, Soultanidis G, et al. Magnetization-prepared GRASP MRI for rapid 3D T1 mapping and fat/water-separated T1 mapping. *Magn Reson Med*. 2021;86(1):97-114. doi:10.1002/mrm.28679
33. Wang N, Cao T, Han F, et al. Free-breathing multitasking multi-echo MRI for whole-liver water-specific T1, proton density fat fraction, and R2* quantification. *Magn Reson Med*. 2021;87(1):120-137. doi:10.1002/mrm.28970
34. Thompson RB, Chow K, Mager D, Pagano JJ, Grenier J. Simultaneous proton density fat-fraction and R2* imaging with water-specific T1 mapping (PROFIT1): application in liver. *Magn Reson Med*. 2020;85(1):223-238. doi:10.1002/mrm.28434
35. Oh J, Han ET, Pelletier D, Nelson SJ. Measurement of in vivo multi-component T2 relaxation times for brain tissue using multi-slice T2 prep at 1.5 and 3 T. *Magn Reson Imaging*. 2006;24(1):33-43. doi:10.1016/j.mri.2005.10.016
36. Akçakaya M, Basha TA, Weingärtner S, Roujol S, Berg S, Nezafat R. Improved quantitative myocardial T2 mapping: impact of the fitting model. *Magn Reson Med*. 2014;74(1):93-105. doi:10.1002/mrm.25377
37. Alonso-Ortiz E, Levesque IR, Pike GB. MRI-based myelin water imaging: a technical review. *Magn Reson Med*. 2014;73(1):70-81. doi:10.1002/mrm.25198
38. Weidlich D, Schlaeger S, Kooijman H, et al. T2 mapping with magnetization-prepared 3D TSE based on a modified BIR-4 T2 preparation. *NMR Biomed*. 2017;30(11):e3773. doi:10.1002/nbm.3773
39. Paul S, Dharnia E, Kedia S. Non-alcoholic fatty liver disease associated with hepatocellular carcinoma: an increasing concern. *Indian J Med Res*. 2019; 149(1):9-17. doi:10.4103/ijmr.IJMR_1456_17
40. Milotta G, Cruz G, Neji R, Prieto C, Botnar R. 3D isotropic-resolution non-rigid motion compensated liver T1, T2 and fat fraction mapping. *Proc Int Soc Magn Reson Med*. 2021;29:1234.
41. Wang N, Serry FM, Cao T, et al. Free-breathing dual-flip-angle multitasking multi-echo (MT-ME-dFA) MRI for whole-liver, B1+ insensitive quantification of T1, PDFF, and R2*. *Proc Int Soc Magn Reson Med*. 2022;30:110.
42. Muslu Y, Cashen TA, Mandava S, Reeder SB. Free-breathing, fat- and B1-corrected T1 mapping of the liver with chemical shift encoded inversion recovery MRI. *Proc Int Soc Magn Reson Med*. 2022;30:115.
43. Siversson C, Tiderius C-J, Neuman P, Dahlberg L, Svensson J. Repeatability of t1-quantification in dGEMRIC for three different acquisition techniques: two-dimensional inversion recovery, three-dimensional Look Locker, and three-dimensional variable flip angle. *J Magn Reson Imaging*. 2010;31(5): 1203-1209. doi:10.1002/jmri.22159
44. Brittain JH, Hu BS, Wright GA, Meyer CH, Macovski A, Nishimura DG. Coronary angiography with magnetization-prepared T2 contrast. *Magn Reson Med*. 1995;33(5):689-696. doi:10.1002/mrm.1910330515
45. Nguyen TD, Deh K, Monohan E, et al. Feasibility and reproducibility of whole brain myelin water mapping in 4 minutes using fast acquisition with spiral trajectory and adiabatic t2prep (FAST-t2) at 3T. *Magn Reson Med*. 2015;76(2):456-465. doi:10.1002/mrm.25877

46. Hedderich D, Weiss K, Spiro J, et al. Clinical evaluation of free-breathing contrast-enhanced t1w MRI of the liver using pseudo golden angle radial k-space sampling. *RöFo*. 2018;190(7):601-609. doi:[10.1055/s-0044-101263](https://doi.org/10.1055/s-0044-101263)
47. Zamskiy M, Weiss K, Harder FN, et al. Isotropic resolution volumetric liver T2 mapping using a free-breathing navigator-gated radial stack-of-stars T2-prepared Dixon acquisition. *Proc Int Soc Magn Reson Med*. 2022;30:2286.
48. Tripp D, Kunze KP, Crabb M, Neji R, Prieto C, Botnar R. Respiratory-motion-corrected simultaneous 3D T1, T2, and fat-fraction mapping at 0.55T, for comprehensive characterization of liver tissue. *Proc Int Soc Magn Reson Med*. 2023;31:56.
49. Rosenzweig S, Scholand N, Holme HCM, Uecker M. Cardiac and respiratory self-gating in radial MRI using an adapted singular spectrum analysis (SSA-FARY). *IEEE Trans Med Imaging*. 2020;39(10):3029-3041. doi:[10.1109/tmi.2020.2985994](https://doi.org/10.1109/tmi.2020.2985994)
50. Feng L, Axel L, Chandarana H, Block KT, Sodickson DK, Otazo R. XD-GRASP: golden-angle radial MRI with reconstruction of extra motion-state dimensions using compressed sensing. *Magn Reson Med*. 2015;75(2):775-788. doi:[10.1002/mrm.25665](https://doi.org/10.1002/mrm.25665)
51. Uecker M, Lai P, Murphy MJ, et al. ESPIRiT—an eigenvalue approach to autocalibrating parallel MRI: where SENSE meets GRAPPA. *Magn Reson Med*. 2013;71(3):990-1001. doi:[10.1002/mrm.24751](https://doi.org/10.1002/mrm.24751)
52. Condat L. A direct algorithm for 1-d total variation denoising. *IEEE Signal Process Lett*. 2013;20(11):1054-1057. doi:[10.1109/lsp.2013.2278339](https://doi.org/10.1109/lsp.2013.2278339)
53. Beck A, Teboulle M. Fast gradient-based algorithms for constrained total variation image denoising and deblurring problems. *IEEE Trans Image Process*. 2009;18(11):2419-2434. doi:[10.1109/tip.2009.2028250](https://doi.org/10.1109/tip.2009.2028250)
54. Stelter JK, Boehm C, Ruschke S, et al. Hierarchical multi-resolution graph-cuts for water-fat-silicone separation in breast MRI. *IEEE Trans Med Imaging*. 2022;41(11):3253-3265. doi:[10.1109/tmi.2022.3180302](https://doi.org/10.1109/tmi.2022.3180302)
55. Eggers H, Brendel B, Duijndam A, Herigault G. Dual-echo Dixon imaging with flexible choice of echo times. *Magn Reson Med*. 2010;65(1):96-107. doi:[10.1002/mrm.22578](https://doi.org/10.1002/mrm.22578)
56. Schlaeger S, Weidlich D, Klupp E, et al. Water t2 mapping in fatty infiltrated thigh muscles of patients with neuromuscular diseases using a t2-prepared 3d turbo spin echo with SPAIR. *J Magn Reson Imaging*. 2019;51(6):1727-1736. doi:[10.1002/jmri.27032](https://doi.org/10.1002/jmri.27032)
57. Mozes FE, Tunncliffe EM, Moolla A, et al. Mapping tissue water t1 in the liver using the MOLLI t1 method in the presence of fat, iron and b0 inhomogeneity. *NMR Biomed*. 2018;32(2):e4030. doi:[10.1002/nbm.4030](https://doi.org/10.1002/nbm.4030)
58. Ruschke S, Karampinos DC. Single-voxel short-TR multi-TI multi-TE STEAM MRS for water-fat relaxometry. *Magn Reson Med*. 2022;87(6):2587-2599. doi:[10.1002/mrm.29157](https://doi.org/10.1002/mrm.29157)
59. Qayyum A. MR spectroscopy of the liver: principles and clinical applications. *RadioGraphics*. 2009;29(6):1653-1664. doi:[10.1148/rg.296095520](https://doi.org/10.1148/rg.296095520)
60. Rocque M. Fully automated contactless respiration monitoring using a camera. In: 2016 IEEE International Conference on Consumer Electronics (ICCE); 2016. doi:[10.1109/ICCE.2016.7430697](https://doi.org/10.1109/ICCE.2016.7430697)
61. S en egas J, Krueger S, Wirtz D, et al. Comparison of liver motion measured by dynamic MRI and respiration signals obtained by an optical sensor. *Proc Int Soc Magn Reson Med*. 2018;26:2528.
62. Harder F, Loh ofer FK, Kaissis GA, et al. Camera-based respiratory triggering improves the image quality of 3d magnetic resonance cholangiopancreatography. *Eur J Radiol*. 2019;120:108675. doi:[10.1016/j.ejrad.2019.108675](https://doi.org/10.1016/j.ejrad.2019.108675)
63. Gottwald LM, Blanken CPS, Tourais J, et al. Retrospective camera-based respiratory gating in clinical whole-heart 4d flow MRI. *J Magn Reson Imaging*. 2021;54(2):440-451. doi:[10.1002/jmri.27564](https://doi.org/10.1002/jmri.27564)
64. Segars WP, Sturgeon G, Mendonca S, Grimes J, Tsui BMW. 4d XCAT phantom for multimodality imaging research. *Med Phys*. 2010;37(9):4902-4915. doi:[10.1118/1.3480985](https://doi.org/10.1118/1.3480985)
65. ITIS Foundation. Tissue properties database v4.1. <https://itis.swiss/virtual-population/tissue-properties/downloads/database-v4-1/>; 2022.
66. Collins CM, Yang B, Yang QX, Smith MB. Numerical calculations of the static magnetic field in three-dimensional multi-tissue models of the human head. *Magn Reson Imaging*. 2002;20(5):413-424. doi:[10.1016/s0730-725x\(02\)00507-6](https://doi.org/10.1016/s0730-725x(02)00507-6)
67. Maril N, Collins CM, Greenman RL, Lenkinski RE. Strategies for shimming the breast. *Magn Reson Med*. 2005;54(5):1139-1145. doi:[10.1002/mrm.20679](https://doi.org/10.1002/mrm.20679)
68. Yu H, Shimakawa A, McKenzie CA, Brodsky E, Brittain JH, Reeder SB. Multiecho water-fat separation and simultaneous r2* estimation with multi-frequency fat spectrum modeling. *Magn Reson Med*. 2008;60(5):1122-1134. doi:[10.1002/mrm.21737](https://doi.org/10.1002/mrm.21737)
69. Bydder M, Yokoo T, Hamilton G, et al. Relaxation effects in the quantification of fat using gradient echo imaging. *Magn Reson Imaging*. 2008;26(3):347-359. doi:[10.1016/j.jmri.2007.08.012](https://doi.org/10.1016/j.jmri.2007.08.012)
70. Nehrke K, B ornert P. DREAM—a novel approach for robust, ultrafast, multislice b1 mapping. *Magn Reson Med*. 2012;68(5):1517-1526. doi:[10.1002/mrm.24158](https://doi.org/10.1002/mrm.24158)
71. Knopp T, Grosser M. MRIReco.jl: an MRI reconstruction framework written in Julia. *Magn Reson Med*. 2021;86(3):1633-1646. doi:[10.1002/mrm.28792](https://doi.org/10.1002/mrm.28792)
72. Knopp T, Boberg M, Grosser M. NFFT.jl: generic and fast Julia implementation of the nonequidistant fast Fourier transform. <https://arxiv.org/abs/2208.00049>; 2022.
73. Ren J, Dimitrov I, Sherry AD, Malloy CR. Composition of adipose tissue and marrow fat in humans by 1H NMR at 7 tesla. *J Lipid Res*. 2008;49(9):2055-2062. doi:[10.1194/jlr.D800010-JLR200](https://doi.org/10.1194/jlr.D800010-JLR200)
74. Hamilton G, Schlein AN, Middleton MS, et al. In vivo triglyceride composition of abdominal adipose tissue measured by 1H MRS at 3T. *J Magn Reson Imaging*. 2017;45(5):1455-1463. doi:[10.1002/jmri.25453](https://doi.org/10.1002/jmri.25453)
75. Ruschke S, Karampinos DC. ALFONSO: a versatile formulation for n-dimensional signal model fitting of MR spectroscopy data and its application in MRS of body lipids. *Proc Int Soc Magn Reson Med*. 2022;30:2776.
76. Dennis JE, Gay DM, Welsch RE. Algorithm 573: NL2sol—an adaptive nonlinear least-squares algorithm [e4]. *ACM Trans Math Softw*. 1981;7(3):369-383. doi:[10.1145/355958.355966](https://doi.org/10.1145/355958.355966)
77. Roberts NT, Hinshaw LA, Colgan TJ, Li T, Hernando D, Reeder SB. B0 and b1 inhomogeneities in the liver at 1.5 t and 3.0 t. *Magn Reson Med*. 2020;85(4):2212-2220. doi:[10.1002/mrm.28549](https://doi.org/10.1002/mrm.28549)
78. Bae ler B, Schaarschmidt F, Stehning C, Schnackenburg B, Maintz D, Bunck AC. Cardiac t2-mapping using a fast gradient echo spin echo sequence—first in vitro and in vivo experience. *J Cardiovasc Magn Reson*. 2015;17(1):67. doi:[10.1186/s12968-015-0177-2](https://doi.org/10.1186/s12968-015-0177-2)
79. Weing artner S, Desmond KL, Obuchowski NA, et al. Development, validation, qualification, and dissemination of quantitative MR methods: overview and recommendations by the ISMRM Quantitative MR Study Group. *Magn Reson Med*. 2021;87(3):1184-1206. doi:[10.1002/mrm.29084](https://doi.org/10.1002/mrm.29084)

80. Kellman P, Hansen MS. T1-mapping in the heart: accuracy and precision. *J Cardiovasc Magn Reson*. 2014;16(1):2. doi:[10.1186/1532-429x-16-2](https://doi.org/10.1186/1532-429x-16-2)
81. Jaubert O, Arrieta C, Cruz G, et al. Multi-parametric liver tissue characterization using MR fingerprinting: simultaneous T1, T2, T2*, and fat fraction mapping. *Magn Reson Med*. 2020;84(5):2625-2635. doi:[10.1002/mrm.28311](https://doi.org/10.1002/mrm.28311)
82. Li Z, Mathew M, Syed AB, et al. Rapid fat-water separated t1 mapping using a single-shot radial inversion-recovery spoiled gradient recalled pulse sequence. *NMR Biomed*. 2022;35(12):e4803. doi:[10.1002/nbm.4803](https://doi.org/10.1002/nbm.4803)
83. Zaitsev M, Maclaren J, Herbst M. Motion artifacts in MRI: a complex problem with many partial solutions. *J Magn Reson Imaging*. 2015;42(4):887-901. doi:[10.1002/jmri.24850](https://doi.org/10.1002/jmri.24850)
84. Velasco C, Cruz G, Jaubert O, Lavin B, Botnar RM, Prieto C. Simultaneous comprehensive liver t1, t2, t2*, t1rho, and fat fraction characterization with MR fingerprinting. *Magn Reson Med*. 2021;87(4):1980-1991. doi:[10.1002/mrm.29089](https://doi.org/10.1002/mrm.29089)
85. Ma D, Gulani V, Seiberlich N, et al. Magnetic resonance fingerprinting. *Nature*. 2013;495(7440):187-192. doi:[10.1038/nature11971](https://doi.org/10.1038/nature11971)
86. Christodoulou AG, Shaw JL, Nguyen C, et al. Magnetic resonance multitasking for motion-resolved quantitative cardiovascular imaging. *Nat Biomed Eng*. 2018;2(4):215-226. doi:[10.1038/s41551-018-0217-y](https://doi.org/10.1038/s41551-018-0217-y)
87. Farrarher SW, Jara H, Chang KJ, Ozonoff A, Soto JA. Differentiation of hepatocellular carcinoma and hepatic metastasis from cysts and hemangiomas with calculated t2 relaxation times and the t1/t2 relaxation times ratio. *J Magn Reson Imaging*. 2006;24(6):1333-1341. doi:[10.1002/jmri.20758](https://doi.org/10.1002/jmri.20758)
88. Low G, Ferguson C, Locas S, et al. Multiparametric MR assessment of liver fat, iron, and fibrosis: a concise overview of the liver “triple screen”. *Abdom Radiol*. 2023;48(6):2060-2073. doi:[10.1007/s00261-023-03887-0](https://doi.org/10.1007/s00261-023-03887-0)
89. Küstner T, Fuin N, Hammernik K, et al. CINENet: deep learning-based 3d cardiac CINE MRI reconstruction with multi-coil complex-valued 4d spatio-temporal convolutions. *Sci Rep*. 2020;10(1):13710. doi:[10.1038/s41598-020-70551-8](https://doi.org/10.1038/s41598-020-70551-8)
90. Terpstra ML, Maspero M, Verhoeff JJC, van den Berg CAT. Accelerated respiratory-resolved 4d-MRI with separable spatio-temporal neural networks. *Med Phys*. 2023;50(9):5331-5342. doi:[10.1002/mp.16643](https://doi.org/10.1002/mp.16643)
91. Henningsson M, Koken P, Stehning C, Razavi R, Prieto C, Botnar RM. Whole-heart coronary MR angiography with 2d self-navigated image reconstruction. *Magn Reson Med*. 2011;67(2):437-445. doi:[10.1002/mrm.23027](https://doi.org/10.1002/mrm.23027)

SUPPORTING INFORMATION

Additional supporting information can be found online in the Supporting Information section at the end of this article.

How to cite this article: Stelter J, Weiss K, Steinhelfer L, et al. Simultaneous whole-liver water T₁ and T₂ mapping with isotropic resolution during free-breathing. *NMR in Biomedicine*. 2024;e5216. doi:[10.1002/nbm.5216](https://doi.org/10.1002/nbm.5216)